Theory of Correlated Chern Insulators in Twisted Bilayer Graphene

Xiaoyu Wang[1,*] and Oskar Vafek[1,2,†]

[1]*National High Magnetic Field Lab, Tallahassee, Florida 32310, USA*

[2]*Department of Physics, Florida State University, Tallahassee, Florida 32306, USA*

(Received 6 December 2023; revised 27 March 2024; accepted 8 May 2024; published 10 June 2024)

Magic-angle twisted bilayer graphene is the best-studied physical platform featuring moiré potential-induced narrow bands with nontrivial topology and strong electronic correlations. Despite their significance, the Chern insulating states observed at a finite magnetic field—and extrapolating to a band filling s at zero field—remain poorly understood. Unraveling their nature is among the most important open problems in the province of moiré materials. Here, we present the first comprehensive study of interacting electrons in finite magnetic field while varying the electron density, twist angle, and heterostrain. Within a panoply of correlated Chern phases emerging at a range of twist angles, we uncover a unified description for the ubiquitous sequence of states with the Chern number t for $(s,t) = \pm(0,4)$, $\pm(1,3)$, $\pm(2,2)$, and $\pm(3,1)$. We also find correlated Chern insulators at unconventional sequences with $s + t \neq \pm 4$, as well as with fractional s, and elucidate their nature.

DOI: 10.1103/PhysRevX.14.021042

Subject Areas: Condensed Matter Physics, Graphene, Strongly Correlated Materials

I. INTRODUCTION

Twisted bilayer graphene (TBG) has been a subject of intense theoretical and experimental investigation, in no small part due to its isolated, topologically nontrivial, narrow bands displaying rich correlated electron physics when partially occupied [1,2]. As the twist angle between the two graphene layers is tuned toward the magic value of approximately 1.05° [3], TBG devices show a plethora of correlated phenomena including superconductivity, correlated insulating states, and (quantized) anomalous Hall effect [4–26]. The nontrivial topology of the pair of narrow bands for a given valley and spin flavor is protected by the combined twofold rotation symmetry about the out-of-plane axis C_{2z} (an emergent symmetry at low twist angle) and spinless time reversal symmetry T [27,28]. The narrow band Hilbert space can thus be decomposed into a Chern $+1$ and a Chern -1 band [27,29,30]. One way to reveal the nontrivial topology of the narrow bands is to break C_{2z} via alignment with the hexagonal boron nitride substrate (h-BN) and separate the Chern bands in energy. If, in addition, the valley is spontaneously polarized, thus breaking T, the resulting state with one electron or hole per moiré unit cell becomes a Chern ± 1 insulator [31–34]. Indeed, experiments have observed the anomalous Hall effect (AHE) near the filling of three electrons per moiré unit cell [10,20] in h-BN aligned samples. Further studies on nonaligned samples [21,25] have also observed AHE near one electron per moiré unit cell. Theoretically, such zero-field Chern insulating states (zCIs) have been proposed to be energetically competitive near magic angle, when the Coulomb interaction exceeds the narrow bandwidth, even without the h-BN alignment [30,33,35,36].

An external magnetic field B, which preserves C_{2z} but breaks T, has been argued to be an alternative way to reveal the band topology [11,19,22], as evidenced by the experimental observations of correlated Chern insulating states (CCIs) with a finite Chern number t and extrapolating to a band filling s at $B = 0$ [6–8,11,13–16,18,19,21–23,25,26]. Specifically, the most prominent sequence of CCIs has $(s,t) = (0,\pm 4), \pm(1,3), \pm(2,2), \pm(3,1)$, consistent with selective population of the aforementioned $B = 0$ Chern $\pm$ 1 bands [11,21,22]. These experiments also report that some CCIs are stable down to $B \sim 1$ T, suggesting that they originate from the zCIs [11,21].

However, CCIs are also observed in TBG devices away from the magic angle (approximately 1.27°), where the bandwidth of the narrow bands is expected to be significantly larger than at 1.05°, without any observation of the correlated insulators at $B = 0$ [9]. Such CCIs appear only above a critical B, below which they transition into nearly compressible states for a fixed (s,t). Similar phenomenology has also been reported in near-magic-angle devices, leading to an alternative explanation of the CCIs

*xiaoyuw@magnet.fsu.edu

†vafek@magnet.fsu.edu

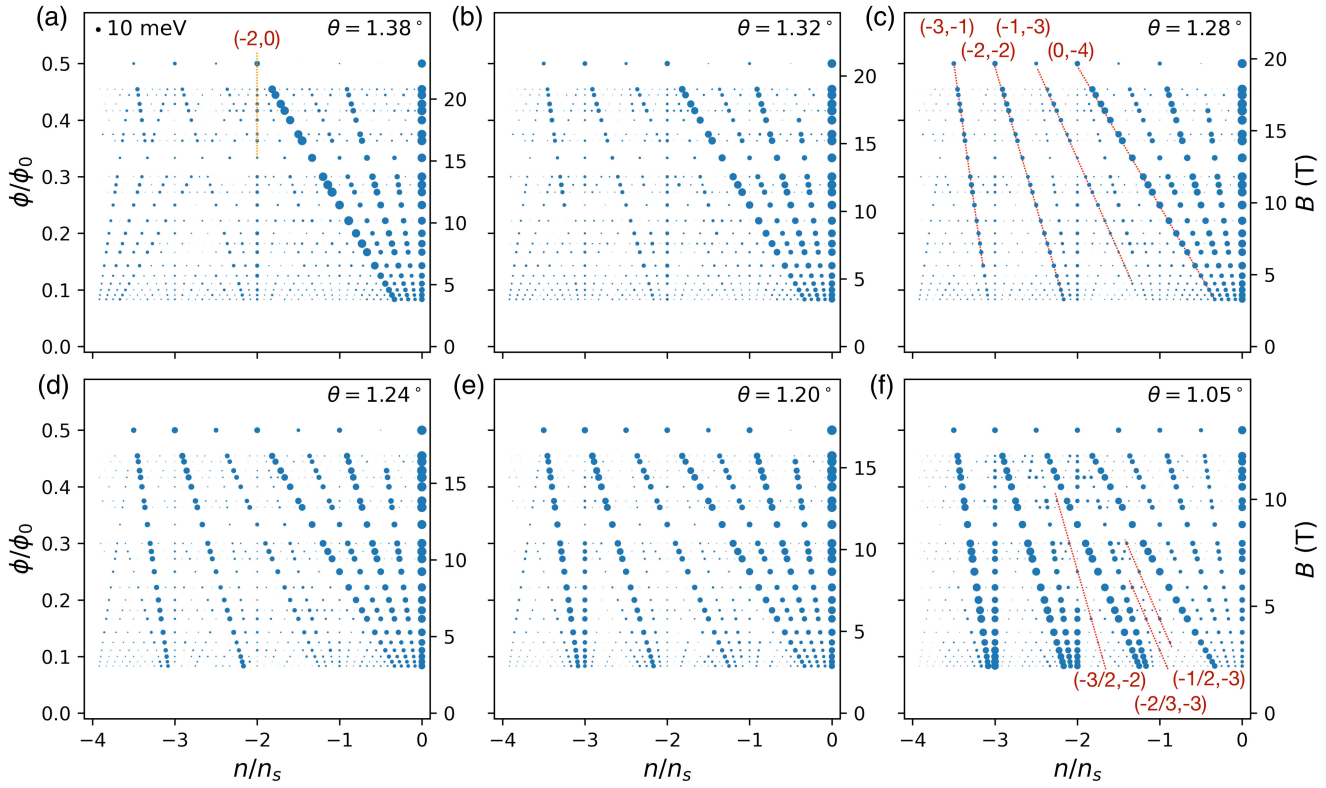

FIG. 1. Single-electron excitation gap as a function of electron filling and magnetic flux in the presence of 0.2% uniaxial heterostrain at twist angles 1.38° (a), 1.32° (b), 1.28° (c), 1.24° (d), 1.2° (e), and 1.05° (f). The sizes of the gaps are proportional to the radius of the respective solid circles, with the circle representation 10 meV shown in (a). The sequences of $(s,t) = (0,-4)$, $(-1,-3)$, $(-2,-2)$, and $(-3,-1)$ are labeled by red dashed lines in (c). Chern insulating states with fractional s at $(s,t) = (-1/2,-3)$, $(-2/3,-3)$, and $(-3/2,-2)$ are labeled by dashed lines in (f). A quantum spin Hall insulating state is identified at high twist angles and labeled by the orange dashed line in (a).

invoking Stoner ferromagnetism within the magnetic subbands [7,15,16,23], termed Hofstadter subband ferromagnets (HSFs) [15]. As argued theoretically [37–39], realistic heterostrain can also increase the bandwidth dramatically near the magic angle, likely placing many TBG devices in the intermediate coupling regime where the zCIs may not be energetically favored.

To date, the nature of these CCIs remains poorly understood. No microscopic calculation favoring zCI, HSF, or other states has been carried out at $B \neq 0$ nor tying them to the relevant experiments. Moreover, the interplay of the CCIs with the competing states at $B = 0$ near the magic angle, such as the intervalley coherent (IVC) states [29,33,40–42], the incommensurate Kekulé spiral (IKS) orders [38], and the stripe and nematic states [14,30,43,44], remains unclear.

Here, we report the first comprehensive study of the interacting electrons within the TBG narrow bands directly at $B \neq 0$ and construct the phase diagram for a range of twist angles, B fields, and electron densities, with and without heterostrain. Consistent with the experimental observations, we find CCIs with $(0, \pm 4)$, $\pm(1,3)$, $\pm(2,2)$, and $\pm(3,1)$, as shown in Fig. 1 for the case with heterostrain and Fig. 2 for the case without heterostrain. These figures plot the single-particle excitation gap at the Fermi level obtained using the self-consistent Hartree-Fock method for each electron density and each magnetic field that we study. In either the strained or unstrained case, CCIs are found to be stabilized at higher B fields for twist angles as high as 1.38° (the highest twist angle studied in this work). Based on an analysis of their wave functions, we identify them as correlated Hofstadter ferromagnets (CHFs). Similar to HSFs, the CHFs correspond to selective population of the valley and spin flavors but of the interaction-renormalized magnetic subbands (see Fig. 3). Unlike HSFs, however, CHFs may include—but are not limited to—spin- and/or valley-polarized states which correspond to $B = 0$ Chern insulators whose interaction renormalized bands are Landau quantized at $B \neq 0$. Although only metastable at $B = 0$, such Chern insulators can be stabilized at $B \neq 0$ in the form of CHFs as we demonstrate in Figs. 6(d) and 6(e).

For realistic heterostrain (Fig. 1), upon lowering B and at a nonzero s we find a phase transition into incompressible states with intervalley coherence. These states break the discrete magnetic translation symmetry but preserve the combination of the discrete magnetic translation and a $U_v(1)$ valley transformation (see Sec. III B) and, therefore,

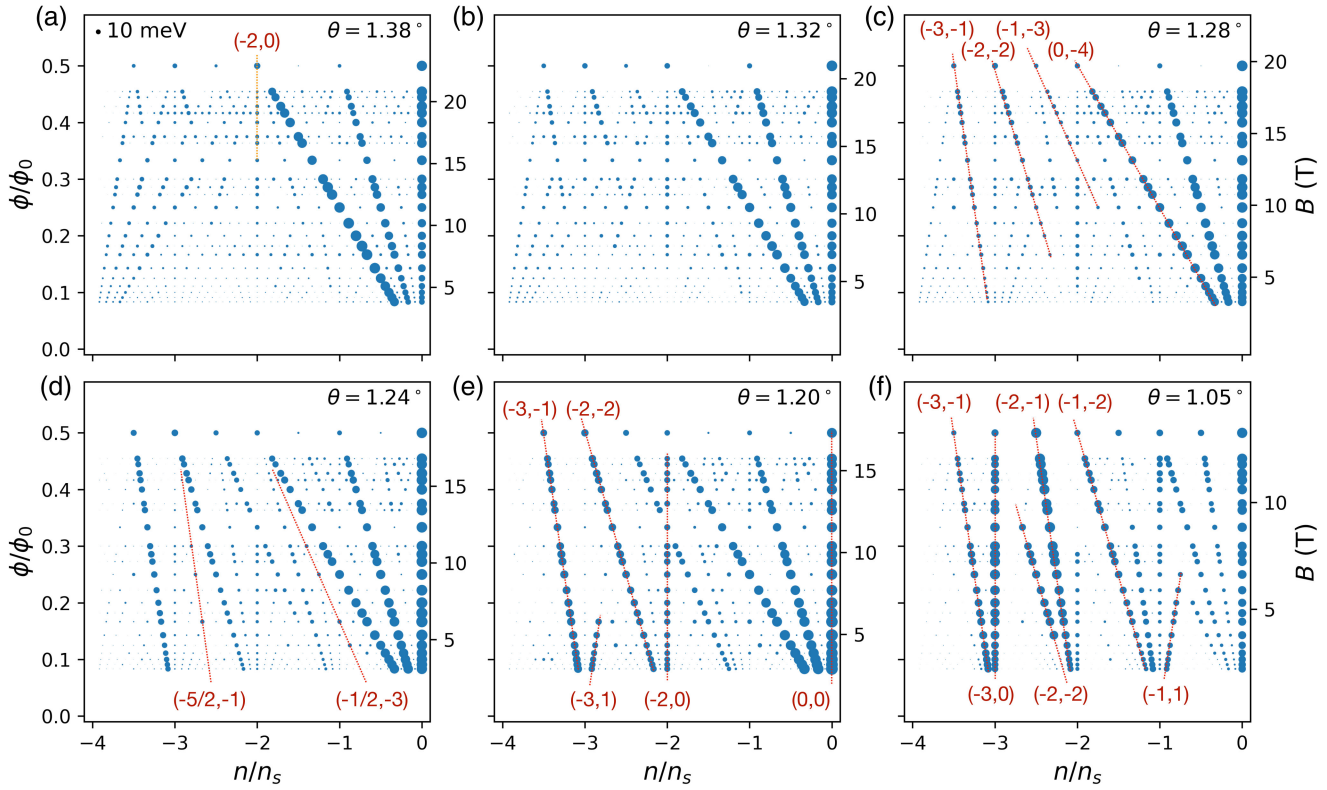

FIG. 2. Single-electron excitation gap as a function of electron filling and magnetic flux in the absence of heterostrain at twist angles 1.38° (a), 1.32° (b), 1.28° (c), 1.24° (d), 1.2° (e), and 1.05° (f). Compared to Fig. 1, results at larger twist angles (upper) are similar, while noted differences emerge at lower twist angles.

are the finite B analogs of the IKS states [38], albeit carrying a nonzero Chern number t. Upon lowering B and at larger twist angles, the IKS states transition into nearly compressible states; at lower twist angles, they remain robust down to the lowest magnetic flux studied in this work.

In the absence of heterostrain (Fig. 2) and at larger twist angles, we instead observe CHFs transitioning directly into nearly compressible states upon lowering B without the intermediate IKS states. As we lower the twist angle toward 1.05°, the incompressible state at $\pm(3,1)$ extends to lower B and crosses over into the finite B analog of the zCI, approaching maximal sublattice polarization. We refer to this state as the strong coupling Chern insulator (sCI). Because there is no symmetry distinction between them, there is no true phase transition between the CHF and the sCI; rather, it is a smooth crossover as shown in Figs. 4(c) and 4(d). The $\pm(2,2)$, $\pm(1,3)$, and $(0,\pm 4)$ states also approach sCIs upon decreasing the twist angle, but they experience a first-order phase transition into IVCs at low twist angles [29,33,40–42]. IVCs break the $U_v(1)$ valley symmetry, but, unlike the IKSs, they preserve the magnetic translation symmetry while also strongly hybridizing the entirety of the narrow band Hilbert space. The details of this transition depend sensitively on the model parameters, as shown in Fig. S19 [45].

Conversely, in the presence of heterostrain, the sCIs are absent in Fig. 1, as evidenced by the fact that the sublattice polarization remains low and far from saturating the sCI bound [Figs. 4(a) and 4(b)]. At the magic angle with heterostrain, we also identify Chern 0 IKS states along $(-3,0)$ and $(-2,0)$ [Fig. 1(f)], consistent with what has been reported previously in $B=0$ Hartree-Fock calculations [38]. Unlike IKS states at a nonzero t, these states are less robust upon increasing B and lose to nearly compressible states. A similar phenomenon has been reported experimentally in Refs. [15,21,22,46].

In addition to these prominent CCIs, we also find gapped Chern states emanating from band edges and the charge neutrality point (CNP) as shown in Figs. 1 and 2. In the presence of heterostrain, they are quantum Hall ferromagnetic states (QHFMs) corresponding to spin-valley symmetry-breaking states within a multiflavored Landau level, with more details discussed in Figs. S6 and S7 [45]. Without heterostrain, gapped states emanating from the band edges are also identified as QHFMs (Fig. S13 [45]). However, the gapped states emanating from the CNP assume a different character (Fig. S14 [45]), developing intervalley coherence and a correlation gap at $B=0$ even at the largest twist angle studied. In contrast, QHFMs are field-induced symmetry-breaking states and are absent at $B=0$. At larger twist angles, a quantum spin

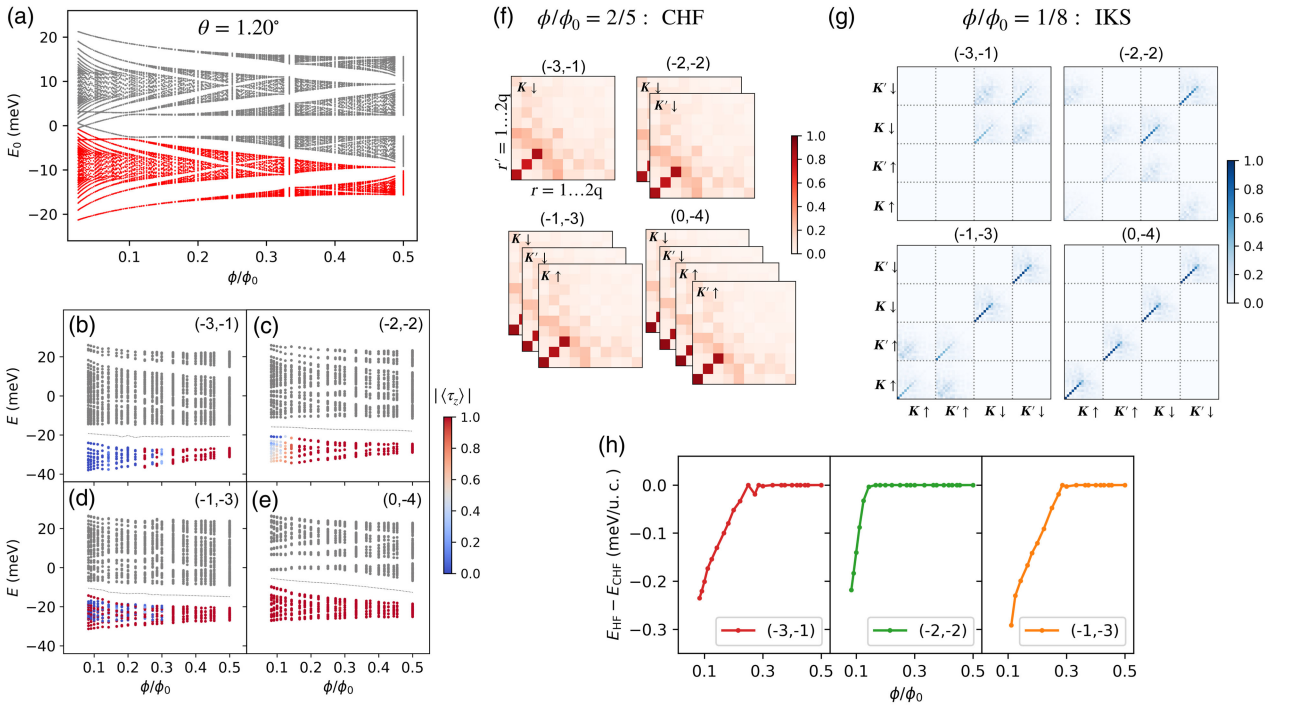

FIG. 3. Compilation of B-SCHF results at $\theta = 1.2°$. (a) The noninteracting spectra. The group of magnetic subbands colored in red has total Chern number -1. (b)–(e) The self-consistent Hartree-Fock spectra along $(s, t) = (-3, -1)$, $(-2, -2)$, $(-1, -3)$, and $(0, -4)$. The occupied electronic states are colored by their valley polarization $|\langle\tau_z\rangle|$. $|\langle\tau_z\rangle| \to 1$ (0) implies maximal valley polarization (maximal intervalley mixing). The alternating colors along $(-3, -1)$ near $\phi/\phi_0 \approx 0.3$ are due to near energetic degeneracies (approximately 0.05 meV) between competing states and are not resolved within our calculation. Along $(-1, -3)$ and at $\phi/\phi_0 < 0.3$, the occupied single-electronic states are maximally valley polarized in the down spin sector and maximally intervalley mixing in the up spin sector. One-particle density matrix at higher B (f) and lower B (g) showing either valley- and spin-polarized state (CHF) or intervalley coherent state (IKS). (h) shows the Hartree-Fock energy difference per moiré unit cell between the ground state and the (metastable) CHF state along $(-3, -1)$, $(-2, -2)$, and $(-1, -3)$.

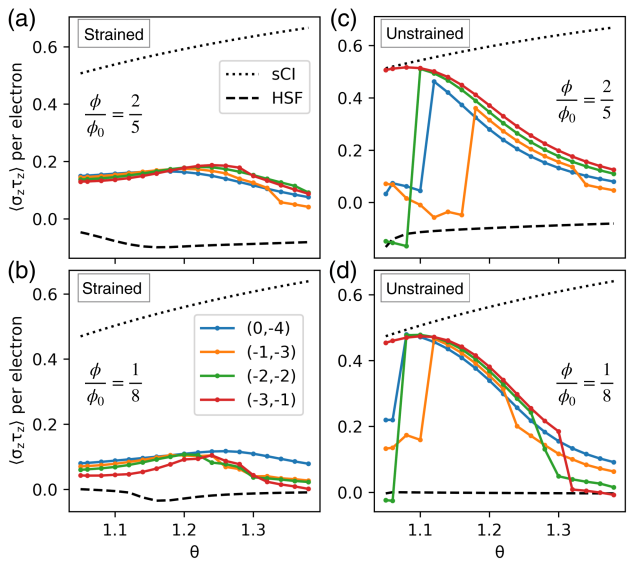

FIG. 4. Averaged $\sigma_z\tau_z$ per occupied single-electron states at $(s, t) = (0, -4)$, $(-1, -3)$, $(-2, -2)$, and $(-3, -1)$ for (a) $\phi/\phi_0 = 2/5$ with heterostrain, (b) $\phi/\phi_0 = 1/8$ with heterostrain, (c) $\phi/\phi_0 = 2/5$ without heterostrain, and (d) $\phi/\phi_0 = 1/8$ without heterostrain. The dotted line is the value for sCI, and the dashed line corresponds to HSF.

Hall insulating state (QSH) along $(-2, 0)$ is identified [see the orange dashed line in Figs. 1(a) and 2(a)], whose origin can be traced back to the spin-split noninteracting magnetic subbands at half flux quantum per moiré unit cell (Figs. S1 and S11 [45]). CCIs extrapolating to a fractional s at $B = 0$ can also be found at 1.05° with heterostrain and for all twist angles in the absence of heterostrain. Further examination of their many-body wave functions reveal that the magnetic translation symmetries are broken (Figs. 7, S9, and S16 [45]), similar to the symmetry-broken Chern insulators discussed in relation to the experiments in Ref. [14].

II. MODEL AND METHOD

We perform self-consistent Hartree-Fock analysis (B-SCHF) at $B \neq 0$ using the minimal continuum Hamiltonian (BM) [3,47], with Coulomb interactions projected onto the narrow band Hilbert space. Here, we briefly outline the formalism; additional details are in Supplemental Material [45]. Our starting point is the (strained) BM Hamiltonian at rational magnetic flux ratios $\phi/\phi_0 = p/q$, where p and q are coprime integers, ϕ is the magnetic flux per moiré unit cell, and $\phi_0 = h/e$ is the

magnetic flux quantum. We choose a Landau gauge such that the magnetic vector potential $\mathbf{A}(\mathbf{r}) = eB\hat{y}$, where $\hat{y}$ is defined along $\mathbf{L}_2$ direction, with $\mathbf{L}_{i=1,2}$ the two (strain-deformed) moiré unit cell vectors. The interacting Hamiltonian is invariant under discrete magnetic translation symmetries $\hat{t}_{\mathbf{L}_1}(\mathbf{r}) = e^{-i2\pi(\phi/\phi_0)(y/|\mathbf{L}_2|)}\hat{T}_{\mathbf{L}_1}$ and $\hat{t}_{\mathbf{L}_2} = \hat{T}_{\mathbf{L}_2}$, where $\hat{T}_{\mathbf{L}_{i=1,2}}$ denote discrete moiré translations at $B = 0$. $\hat{t}_{\mathbf{L}_1}$ and $\hat{t}_{\mathbf{L}_2}$ are noncommuting but satisfy $[\hat{t}_{\mathbf{L}_1}\hat{t}^q_{\mathbf{L}_2}] = 0$. This allows us to define a magnetic Brillouin zone described by the magnetic crystal momentum $\mathbf{k} = k_1\mathbf{g}_1 + k_2\mathbf{g}_2$, with $k_1 \in [0, 1)$ and $k_2 \in [0, 1/q)$, and $\mathbf{g}_{i=1,2}$ are moiré reciprocal lattice vectors (for more detailed information, see Supplemental Material, Secs. I and II [45]). We therefore first solve for the noninteracting Hofstadter spectra $\varepsilon_{\eta sr}(\mathbf{k})$ and associated eigenstates $|\Psi_{\eta sr}(\mathbf{k})\rangle$, with $\eta = \mathbf{K}, \mathbf{K}'$ and $s = \uparrow, \downarrow$ denoting valley and spin quantum numbers, respectively, and $r = 1, \ldots 2q$ is the magnetic subband index. Spin Zeeman splitting is also considered in this calculation. In earlier works [48,49], we used the hybrid Wannier states (hWS) at $B = 0$ to construct the finite B Hilbert space. Although accurate and numerically efficient at low B, the hWS approach to TBG was shown to break down above moderate flux ratios (e.g., $\phi/\phi_0 \gtrsim 0.2$) [48]. As one of the purposes of this work is to connect the CCIs between low and high B, we instead solve the BM Hamiltonian by expanding in Landau level (LL) basis of each graphene layer. By scaling the upper Landau level cutoff as ϕ/ϕ_0 decreases, we ensure an accurate construction of the Hilbert space as well as the noninteracting Hofstadter spectra. While the high-B regime is straightforward in the LL basis, the low B is computationally expensive. We were nevertheless able to reach $\phi/\phi_0 = 1/12$ using the LL basis, which corresponds to approximately 2.2 T at the magic angle (for all twist angles studied here, we reach $B < 4$ T). This value is, therefore, sufficiently low to make direct comparison with experiments. The (interacting) results shown in Figs. 1 and 2 are for $1/12 \leq \phi/\phi_0 \leq 1/2$, with the maximum value of q being 12 and $1 < p < q$.

For the model parameters studied in this work, the gap to remote Hofstadter bands does not close at the magnetic fluxes of interest. We study interaction effects by projecting the screened Coulomb interaction onto the narrow band Hilbert space. The Hamiltonian is given by

$$H = \sum_{\eta sr,\mathbf{k}} \varepsilon_{\eta sr}(\mathbf{k}) d^\dagger_{\eta sr,\mathbf{k}} d_{\eta sr,\mathbf{k}} + \frac{1}{2A}\sum_{\mathbf{q}} V_{\mathbf{q}} \delta\hat{\rho}_{\mathbf{q}} \delta\hat{\rho}_{-\mathbf{q}}. \quad (1)$$

Here, A is the total area of the system, $d_{\eta sr,\mathbf{k}}$ is the electron annihilation operator, and $\delta\hat{\rho}_{\mathbf{q}}$ is the Fourier transform of the electron density operator projected onto the narrow bands, subtracting a background charge density [48,50,51]. It is given by

$$\delta\hat{\rho}_{\mathbf{q}} = \sum_{\eta s,rr',\mathbf{k},\mathbf{p}} \langle \Psi_{\eta sr}(\mathbf{k})|e^{-i\mathbf{q}\cdot\mathbf{r}}|\Psi_{\eta sr'}(\mathbf{p})\rangle \times \left(d^\dagger_{\eta sr,\mathbf{k}} d_{\eta sr',\mathbf{p}} - \frac{1}{2}\delta_{r,r'}\delta_{\mathbf{k},\mathbf{p}} \right). \quad (2)$$

We consider a dual-gate screened Coulomb interaction of the form $V(\mathbf{q}) = (2\pi e^2/\epsilon_0\epsilon_r|\mathbf{q}|)\tanh(|\mathbf{q}|\xi/2)$, with relative dielectric constant $\epsilon_r = 15$ and screening length $\xi = 4\sqrt{|\mathbf{L}_1||\mathbf{L}_2|}$. These parameters are chosen to match the overall change of chemical potential from empty to full occupation of the narrow bands in magic-angle devices as extracted from the compressibility measurements as well as STM [6,7,52–54] (see also Fig. S2 [45]).

In the B-SCHF procedure, we minimize the total energy for a fixed particle number using many-body wave functions expressible as product states:

$$|\Omega\rangle = \prod_{n,\mathbf{k}}{}' \left(\sum_{sr} \alpha^{(n)}_{sr,\mathbf{k}} d^\dagger_{\mathbf{K}sr,\mathbf{k}} + \sum_{s'r'} \beta^{(n)}_{s'r',\mathbf{k}+\mathbf{q}_0} d^\dagger_{\mathbf{K}'s'r',\mathbf{k}+\mathbf{q}_0} \right)|0\rangle, \quad (3)$$

where $\mathbf{q}_0$ is an arbitrary wave vector shift between single-electron states in opposite valleys, whose value is constrained by the discrete momentum mesh such that $\mathbf{k} + \mathbf{q}_0$ is on the same momentum mesh as $\mathbf{k}$ (modulo a reciprocal lattice vector). The constrained product $\prod'_{n,\mathbf{k}}$ is over all the occupied states labeled by n, $\mathbf{k}$. $\{\alpha^{(n)}_{sr,\mathbf{k}}, \beta^{(n)}_{s'r',\mathbf{k}+\mathbf{q}_0}\}$ are variational parameters that minimize the total energy, and they obey $\sum_{sr}|\alpha^{(n)}_{sr,\mathbf{k}}|^2 + \sum_{s'r'}|\beta^{(n)}_{s'r',\mathbf{k}+\mathbf{q}_0}|^2 = 1$ for any $\{n, \mathbf{k}\}$. The total energy is also optimized with respect to $\mathbf{q}_0$, allowing us to probe IKS-like states (see Supplemental Material, Sec. III D [45]). An equivalent formulation of the B-SCHF procedure (for details, see Supplemental Material, Sec. III [45]) is based on the one-particle density matrix:

$$\hat{Q}_{\eta sr,\eta' s'r'}(\mathbf{k}) \equiv \langle\Omega|\tilde{d}^\dagger_{\eta sr,\mathbf{k}} \tilde{d}_{\eta' s'r',\mathbf{k}}|\Omega\rangle, \quad (4)$$

where for notational convenience we define $\tilde{d}^\dagger_{\mathbf{K}sr,\mathbf{k}} \equiv d^\dagger_{\mathbf{K}sr,\mathbf{k}}$ and $\tilde{d}^\dagger_{\mathbf{K}'s'r',\mathbf{k}} \equiv d^\dagger_{\mathbf{K}'s'r',\mathbf{k}+\mathbf{q}_0}$. Note that $\hat{Q}$ contains information about $\mathbf{q}_0$. In the remaining text, we discuss the numerical results based on either the one-particle density matrix or the many-body wave function, whichever is more convenient.

The projected Hamiltonian at $B \neq 0$ is invariant under the following set of symmetries [50,55,56]: C_{2z}, valley $U_v(1)$ and spin $U_s(1)$, many-body particle-hole P, and magnetic translation symmetries generated by $\hat{t}_{\mathbf{L}_1}$ and $\hat{t}_{\mathbf{L}_2}$. We fix the gauge such that

$$\hat{t}_{\mathbf{L}_1} d^\dagger_{\eta sr,\mathbf{k}} \hat{t}^{-1}_{\mathbf{L}_1} = e^{-i2\pi k_1} d^\dagger_{\eta sr,\mathbf{k}}, \quad (5)$$

$$\hat{t}_{\mathbf{L}_2} d^\dagger_{\eta sr,\mathbf{k}} \hat{t}^{-1}_{\mathbf{L}_2} = e^{-i2\pi k_2} d^\dagger_{\eta sr,\mathbf{k}+\phi/\phi_0\mathbf{g}_1}. \quad (6)$$

The above gauge choice is useful in identifying a magnetic translation symmetry breaking from the density matrix (see Supplemental Material [45]).

In the absence of heterostrain, C_{3z} and $C_{2y}T$ also leave H invariant. P guarantees symmetry about the charge neutrality point, and, therefore, we present our results for the hole filling only.

The B-SCHF calculation is carried out for a range of twist angles from 1.38° to 1.05°, both for the unstrained model as well as for realistic uniaxial heterostrain magnitude $\epsilon = 0.2\%$ and orientation $\varphi = 0°$ (see Supplemental Material [45] and Ref. [39] for the definition of the uniaxial strain orientation). We choose the Fermi velocity such that $\hbar v_F/a = 2482$ meV with the graphene lattice constant $a \approx 2.46$ Å and interlayer tunneling parameters $w_0 = 77$ meV (intrasublattice) and $w_1 = 110$ meV (intersublattice). These parameters place the magic angle near 1.05°. The respective noninteracting Hofstadter spectra and Wannier diagrams with and without heterostrain are shown in Figs. S1 and S11 [45].

At a given B and electron density, obtaining the true Hartree-Fock ground state is a highly nontrivial task due to competing states of similar energy. We typically run about six random initializations of the single-particle density matrix, as well as several educated guesses (e.g., flavor-polarized or intervalley coherent states), and report the lowest-energy state as the ground state. Optimal damping algorithm is also used to speed up the numerical convergence [29]. This elaborate procedure turns out to be adequate (i.e., random and educated initializations converge to the same state) for establishing incompressible ground states with big excitation gaps, such as the CCIs with $(s,t) = (0,\pm 4)$, $\pm(1,3)$, $\pm(2,2)$, and $\pm(3,1)$, QHFMs, and CCIs extrapolating to a fractional s. However, it may face convergence issues for nearly compressible states, which are abundant in the phase diagrams shown in Figs. 1 and 2. We make no assertions regarding the nature of such nearly compressible states in this paper and mainly use them in order to highlight the contrast with the ground states with large excitation gaps or, at $B = 0$, to elucidate the physics of the B-induced incompressible states as in Figs. 6(a)–6(c). We often find competing states close in energy, with $\lesssim 1$ meV difference in the Hartree-Fock energy per moiré unit cell. Throughout the paper, we try to adopt the philosophy of identifying these competing states [2] and comment on how small variations in model parameters (e.g., dielectric constant or kinetic terms beyond BM Hamiltonian) may tip the balance between ground states and metastable states.

III. RESULTS

A. Phase diagram and main CCIs

We first address the finite B phase diagram for TBG subject to 0.2% of heterostrain. Figure 1 gives an overview of the calculated single-particle excitation gap (i.e., the charge gap) as a function of moiré unit cell filling (n/n_s) and magnetic flux ratio (ϕ/ϕ_0) for six twist angles: 1.38°, 1.32°, 1.28°, 1.24°, 1.20°, and 1.05°. The size of the gap is proportional to the radius of the solid circle. As seen, there is a rich panoply of correlated insulating states. We start by focusing on the sequence of CCIs with $(s,t) = (0,-4),(-1,-3),(-2,-2),(-3,-1)$, which are observed for all the twist angles studied and marked by red dashed lines in Fig. 1(c). At larger twist angles, CCIs along $(-3,-1),(-2,-2),(-1,-3)$ emerge at high ϕ/ϕ_0 and are replaced by nearly compressible states at lower ϕ/ϕ_0 via a first-order phase transition. As the twist angle is lowered, they become more robust and can persist beyond the lowest flux ratio of $1/12$ studied in this work.

To better elucidate their nature, we compile detailed results for a representative twist angle 1.20° in Fig. 3. Results for other twist angles can be found in Supplemental Material [45]. Figure 3(a) shows the noninteracting spectra of valley $\mathbf{K}$ and for one spin component (neglecting the Zeeman effect). The magnetic subbands marked in red denote the Chern -1 group below the charge neutrality point. The analogous group of subbands above the charge neutrality point is related to it by particle hole symmetry and also carries total Chern number -1. The remaining two subbands emanate from either the zeroth Landau levels (zLLs) of the energetically split Dirac points ($\phi/\phi_0 \gtrsim 0.1$) or the ± 1 LLs ($\phi/\phi_0 \lesssim 0.1$) and carry Chern number $+1$ each, such that the total Chern number of all magnetic subbands is zero.

Figure 3(b) shows the single-particle spectra including Coulomb interactions along $(s,t) = (-3,-1)$, where the occupied states are colored according to their valley polarization $|\langle \tau_z \rangle|$, where τ_z is the Pauli matrix acting on valley degrees of freedom. $|\langle \tau_z \rangle| \to 1$ (0) implies maximal valley polarization (maximal intervalley mixing). At $\phi/\phi_0 \gtrsim 1/3$, the occupied states are maximally valley polarized and have a large overlap onto the states marked in red in Fig. 3(a). To quantify the overlap, we make use of the density matrix defined in Eq. (4), which has the spin-valley diagonal form $\mathcal{Q}^{(\eta s)}_{r,r'}(\mathbf{k})\delta_{\eta,\eta'}\delta_{s,s'}$ for a state with unbroken valley and spin symmetries. A representative $|\mathcal{Q}^{\mathbf{K}\uparrow}_{r,r'}(\mathbf{0})|$ is shown in Fig. 3(f). It is predominantly diagonal in the magnetic subband index, mostly occupying the lower $q-p$ magnetic subbands, i.e., the group states with total Chern number -1 marked red in Fig. 3(a). For $(-2,-2)$ and $(-1,-3)$ and at higher B, the CCIs are also valley and spin polarized, similarly mostly populating the lower Chern -1 group of magnetic subbands for the specified valley and spin, with $|\mathcal{Q}^{(\eta s)}(\mathbf{0})|$ identical for all occupied flavors. Although these CCIs are closely related to the HSFs discussed in Refs. [7,15,23], the band structure renormalization is apparent in the nonvanishing off-diagonal matrix elements of $\mathcal{Q}^{(\eta s)}_{r,r'}(\mathbf{k})$, signifying hybridization with the

higher-energy subbands [marked by gray in Fig. 3(a)]. For this reason, we refer to them as CHFs. As further demonstrated in Fig. S3 [45], the density matrices of the CHFs assume a much simpler structure when expressed in the eigenbasis of the valley- and spin-symmetric $(0,-4)$ Chern insulating state, which limits to an interaction-renormalized semimetal at $B=0$ (see Fig. S2 [45] and also Ref. [38]).

At lower B, the valley- and spin-polarized CCIs along $(-3,-1)$, $(-2,-2)$, and $(-1,-3)$ all transition into gapped states with strong intervalley mixing, as reflected by $|\langle\tau_z\rangle|\to 0$ for the occupied states shown in Figs. 3(b)–3(e). Along $(-3,-1)$ and $(-1,-3)$, the intervalley mixing is between the same spin species [Fig. 3(g)], and the resulting states do not suffer from the Zeeman energy cost compared to CHFs which have the same spin polarization. However, along $(-2,-2)$, the intervalley mixing is between opposite spins (mixing between the same spins is achieved as a metastable state), leading to an extra Zeeman energy cost. This likely explains the lowered critical field for the transition between the CHF and the IKS states for $(-2,-2)$ compared to $(-3,-1)$ and $(-1,-3)$, as seen in Figs. 3(b)–3(e) by the valley polarization of occupied single-electron states. Based on a detailed analysis of the density matrix, we identify these intervalley coherent CCIs as the finite B analog of IKS states [38] carrying a finite Chern number. We postpone a detailed discussion of identifying IKS states to Sec. III B. Finally, in Fig. 3(h), we show the Hartree-Fock energy difference between the ground state and the CHFs which become metastable at lower B. It shows that the phase transition between CHF and IKS is likely first order along $(-3,-1)$ and $(-1,-3)$, where the IKS order parameter—qualitatively captured by the $|\hat{Q}_{\mathbf{K}sr,\mathbf{K}'sr'}(\mathbf{k})|$—has an abrupt onset upon lowering B. On the other hand, the transition along $(-2,-2)$ is most likely second order, as $|\hat{Q}_{\mathbf{K}sr,\mathbf{K}'sr'}(\mathbf{k})|$ gradually increases as B decreases.

The qualitative picture described above is universal across all the twist angles we have studied (see Fig. S4 [45]). However, at larger twist angles, in addition to the phase transition between CHF and IKS, upon further decreasing B we observe a transition from a gapped IKS into a nearly compressible state, e.g., along $(-3,-1)$ at 1.38° as shown in Fig. 1(a). This can be attributed to the larger noninteracting bandwidth and comparatively weaker Coulomb interaction.

B. IKS states

In previous Hartree-Fock studies at $B=0$, a notable finding is that, in the presence of a small amount of uniaxial heterostrain (e.g., 0.2%), the ground state at integer filling fractions are the incommensurate Kekulé spiral ordered states [38]. Unlike the IVC states achieved when heterostrain is absent [29,40], IKS states predominantly mix the lower-energy bands (instead of the full narrow band Hilbert space) between opposite valleys of the noninteracting BM Hamiltonian while developing a wave vector $\mathbf{Q}_{\mathrm{IKS}}$ incommensurate with the underlying moiré lattice. On the moiré scale, a modified discrete translation symmetry is preserved, i.e., discrete moiré translations $(\hat{T}_{\mathbf{L}_{j=1,2}})$ followed by a $U_v(1)$ valley transformation: $e^{-(i/2)(\mathbf{Q}_{\mathrm{IKS}}\cdot\mathbf{L}_j)\tau_z}\hat{T}_{\mathbf{L}_j}$.

In our calculations, we find that the gapped states along $(-3,-1)$, $(-2,-2)$, and $(-1,-3)$ at lower B [Figs. 3(b)–3(e) and 3(g)] also hybridize electronic states predominantly of the lower Chern -1 group of the noninteracting magnetic subbands, break the magnetic translation symmetries generated by $\hat{t}_{\mathbf{L}_{j=1,2}}$, but preserve a modified translation $e^{-(i/2)(\mathbf{Q}_{\mathrm{IKS}}\cdot\mathbf{L}_j)\tau_z}\hat{t}_{\mathbf{L}_j}$. This further constrains the many-body wave function in Eq. (3) and the density matrix in Eq. (4), with details discussed in Supplemental Material, Sec. III D [45]. Therefore, we can identify them as the finite B analog of the zero B IKS states. At larger twist angles, we find only gapped IKS states with a finite Chern number (i.e., nonzero t), and an absence of Chern 0 IKS states. The latter occur only close to the magic angle [e.g., Figs. 1(e) and 1(f)] along $(-3,0)$ and $(-2,0)$. At higher B, these Chern 0 IKS states become energetically unfavorable and lose to nearly compressible states. This phenomenon has been reported in various experiments [15,21,22,46].

C. Robustness of the CHF-IKS phase transition against perturbations

Given the small energy differences between the CHF and IKS states along $(-3,-1)$, $(-2,-2)$, and $(-1,-3)$ shown in Fig. 3(h), it is natural to ask how robust this phase transition is to small variations in model parameters. Although this is difficult to answer definitively, it is possible to present some qualitative arguments favoring such a phase transition. Along $(-2,-2)$, as argued above, Zeeman coupling is expected to favor a CHF state, as it is fully spin polarized, while the IKS is not. The Zeeman energy cost of both CHF and IKS can be computed via $g_s\mu_B\mathrm{tr}\{\hat{Q}s_z\}$, where $g_s=2$, μ_B is the Bohr magneton, and s_z is the z component of the spin. We find that numerically switching off the Zeeman splitting increases the critical field at which the CHF-IKS transition occurs. Interestingly, the same argument does not hold along $(-3,-1)$ and $(-1,-3)$, as IKS does not suffer from extra Zeeman energy cost compared to CHF. It would appear that the relative strength of the Coulomb interaction and the noninteracting bandwidth of the relevant magnetic subbands [red colored states in Fig. 3(a)] also plays an important role. We find numerical evidence that decreasing the Coulomb interaction (e.g., changing the relative dielectric constant from 15 to 25) makes IKS more stable and increases the critical field; conversely, increasing Coulomb interaction favors a CHF state. Finally, there is also evidence that increasing the strength of the uniaxial heterostrain (e.g., from 0.2% to 0.3%) favors IKS over CHF and increases the critical field.

In a recent experiment, the spin polarizations of the main CCIs near the magic angle are identified by edge conductance measurements, with $(-3,-1)$ and (2,2) being spin polarized and $(-2,-2)$ being spin unpolarized [17]. Our theory naturally recovers the spin polarization along $(-3,-1)$. While CHF is fully spin polarized, as mentioned, the IKS is not. Therefore, spin polarization along $\pm(2,2)$ could be used to differentiate between CHF and IKS states as shown in Figs. 3(f) and 3(g). The experimental results, therefore, suggest an IKS state along $(-2,-2)$ and CHF along (2,2), although to fully explain them more careful analysis of the edge modes and modeling beyond the BM Hamiltonian [57] which captures the particle-hole asymmetry are necessary.

D. Crossover to strong coupling regime

In order to clarify the connection between the CHFs and the sCIs, we first note that the sCIs saturate the expectation value of $\sigma_z\tau_z$ for the occupied electronic states, where σ_z and τ_z are Pauli matrices acting in the sublattice and valley subspace, respectively [29,30,48,50]. The solid lines in Figs. 4(a) and 4(b) show calculated $\langle\sigma_z\tau_z\rangle$ per electron as a function of twist angle in the presence of heterostrain along $(0,-4)$, $(-1,-3)$, $(-2,-2)$, and $(-3,-1)$, for $\phi/\phi_0 = 2/5$ and $1/8$, respectively. For comparison, the upper dashed line corresponds to the sCI limit and the lower dashed line to the HSF limit. This measure shows that the CHFs are quantitatively different from both the HSFs and the sCIs in the presence of heterostrain but closer to HSFs. Intuitively, the increased $\langle\sigma_z\tau_z\rangle$ of CHFs compared to HSFs may originate in the short-ranged part of the Coulomb repulsion disfavoring two electrons sitting close to each other in real space.

On the other hand, in the absence of heterostrain, as shown in Figs. 4(c) and 4(d), the CHFs along $(-3,-1)$ smoothly cross over into the sCIs upon lowering the twist angle. For our model parameters, there is a collapse of the $\langle\sigma_z\tau_z\rangle$ along $(-2,-2)$, $(-1,-3)$, and $(0,-4)$ at lower twist angles, when the CHFs become energetically less favorable than populating the Landau quantized excitation spectra of the IVC states [33,40,48,58]. As further demonstrated in Fig. S19 [45], this transition depends sensitively on model parameters and can be pushed toward lower ϕ/ϕ_0 (e.g., by moving toward the chiral limit; see Supplemental Material [45] and Ref. [59]). References [11,21] report that the (2,2) persist down to $\phi/\phi_0 \sim 1/25$ and, therefore, argue that they correspond to the zCIs (more precisely, sCIs). Our quantitative calculations clearly demonstrate that such states can indeed be stabilized at weak fields by small changes of the model parameters.

In our earlier work [48], we computed the single-particle excitations of IVC insulators in the strong coupling limit at $B \neq 0$, which have been demonstrated to be the ground states at the CNP and $n/n_s = -2$. At the CNP and at low B, we find twofold degenerate LLs $0, \pm 2, \pm 4, \ldots$. At $n/n_s = \pm 2$, we find instead $0, \pm 1, \pm 2, \ldots$. These have been corroborated by other works [58,60]. Although the results in Ref. [48] assumed adding a single electron or a single hole, they are expected to hold at an asymptotically low B even at a small but finite density along $(0,t)$ or $(\pm 2,t)$. This is because the energy difference between competing many-body states due to addition of a small density of carriers necessary to fill the excited LLs is expected to be proportional to the number of flux quanta, while the energy difference between competing states at $B = 0$ is extensive and thus proportional to the total particle number. Therefore, a finite critical B field would be necessary to tip the energy balance in favor of a state such as the sCI, distinct from the one obtained by a naive rigid filling of the LLs. Closer examination of Fig. 2(f) indeed demonstrates this. At $n/n_s = -2$, we find a prominent $(-2,-1)$ which corresponds to emptying one energetically well-separated LL from the spectra of the $(-2,0)$ IVC state, consistent with our earlier studies. Along $(-2,-2)$ and at $\phi/\phi_0 < 1/7$, a weaker gapped state is observed where two LLs are emptied. However, at $\phi/\phi_0 > 1/7$ and $\phi/\phi_0 \leq 1/3$, the sCI is stabilized via a first-order phase transition. At $n/n_s = 0$, we similarly find a prominent $(0,-2)$ corresponding to emptying a twofold degenerate LL of the (0,0) state [with $(0,-1)$ being the QHFM of $(0,-2)$]. Interestingly, gapped states along $(0,-4)$—expected based on the results in Ref. [48]—are not observed down to $\phi/\phi_0 = 1/12$. Given that this corresponds to an electron filling of $n/n_s = -1/3$, we attribute the absence of $(0,-4)$ to band renormalization effects at finite electron densities not captured in Ref. [48]. Figure 2(f) also shows gapped states emanating from $n/n_s = -3$ and -1 that can be characterized either as sCIs $[(-3,-1), (-1,\pm 1)]$ or via (de)population of the sCIs' Landau quantized excitation spectra $[(-3,0), (-1,-2), (-1,0)]$. We refer interested readers to details presented in Fig. S18 [45]. We note that in the strong coupling limit there are near degeneracies between competing states. For example, along $(-1,-3)$, a Chern -3 sCI can be found as a metastable state, with a Hartree-Fock energy $\lesssim 0.01$ meV higher than the nearly compressible state plotted in Fig. 2(f).

E. Main CCIs in the absence of heterostrain

Though most of the experiments so far are believed to be strongly influenced by uniaxial heterostrain, there are a few experiments which appear to be in the ultralow heterostrain regime [12,18]. In addition to the main CCIs along $(0,\pm 4)$, $\pm(1,3)$, $\pm(2,2)$, and $\pm(3,1)$, these experiments show that the CNP develops a gap at $B = 0$ at low temperatures without any apparent h-BN alignment. This is in contrast to a (gapless) semimetal found at a moderate amount of uniaxial heterostrain (e.g., 0.2%) [12,38]. As discussed in the previous section, in the strong coupling limit, there are prominent gapped states along $(-2,-1)$, while $(-1,-3)$ and $(0,-4)$ are gapless at reasonable magnetic flux ratios. In contrast, $(-2,-1)$ does not appear to be a prominent

gapped state in experiments without h-BN alignment, and the main CCIs are ubiquitous. We therefore conclude that the above low heterostrain experiments [12,18] cannot be in the strong coupling regime with a negligible noninteracting bandwidth.

We investigate the impact of a finite noninteracting bandwidth by systematically studying the finite B phase diagram for a range of twist angles from 1.38° down to the magic angle of 1.05°, in an analogous fashion compared to studies with 0.2% heterostrain. The single-electron excitation gaps at different twist angles, electron densities, and B field are presented in Fig. 2. Through separate $B = 0$ Hartree-Fock calculations, we demonstrate that at CNP the ground state is a gapped IVC state for all twist angles, albeit with an IVC order parameter localized to the vicinity of the $\mathbf{K}$ points of the moiré Brillouin zone at larger twist angles. At the largest twist angle 1.38° with the largest noninteracting bandwidth, the gap structures are very similar to that in the presence of heterostrain. Main CCIs along $(-3,-1)$, $(-2,-2)$, and $(-1,-3)$ first emerge at high B and lose to nearly compressible states at lower B. Here, the main CCIs are CHFs, without competing IVC states nearby. As the twist angle decreases and the noninteracting bandwidth decreases, the main CCIs become stable at lower B. Finally, at the magic angle 1.05° where the noninteracting bandwidth is negligibly small in the BM model, main CCIs along $(-3,-1)$ remain stable, but along $(-2,-2)$ they are stable only for intermediate B fields. Along $(-1,-3)$, we do not observe gapped states. Moreover, we identify a strong $(-2,-1)$ gapped state consistent with previous works [48,58,60]. However, the gapped state along $(0,-4)$ is missing, and we attribute it to a finite B and finite electron density regime where populating the rigid excitation spectra of $n/n_s = 0$ IVC insulator is no longer energetically favorable.

At the twist angle 1.2°, as shown in Fig. 2(e), the main CCIs along $(-3,-1)$, $(-2,-2)$, and $(-1,-3)$ remain robust down to the lowest magnetic flux ratio $\phi/\phi_0 = 1/12$ studied. Simultaneously there are strong IVC states along (0,0) and $(-2,0)$. We also do not find a strong gapped state along $(-2,-1)$. Moreover, the main gapped states emanating from the CNP are along (0,0), $(0,-2)$, and $(0,-4)$, consistent with the mentioned experiments. To better understand these states, we present their detailed Hartree-Fock spectra and representative density matrices in Fig. 5. At $n/n_s = 0$ and along (0,0), the IVC state hybridizes $\{\mathbf{K},\uparrow(\downarrow)\}$ with $\{\mathbf{K}',\downarrow(\uparrow)\}$, creating bonding and antibonding states. The occupied bonding states have net Chern number 0, resulting in the gapped state along (0,0). In contrast, the gapped state along $(0,-4)$ is a CHF, where the occupied group of states in each valley and spin sector contributes a Chern number -1. Along $(0,-2)$, we identify the gapped state as a CHF in the spin $\uparrow$ sector which accounts for the net Chern number -2 and an IVC in the spin $\downarrow$ sector having zero Chern number. Analogously at $n/n_s = -2$, the gapped state along $(-2,0)$ forms intervalley coherence between $\{\mathbf{K},\downarrow\}$ and $\{\mathbf{K}',\downarrow\}$, whereas the gapped state along $(-2,-2)$ is a CHF. Along $(-2,-1)$, we find that the

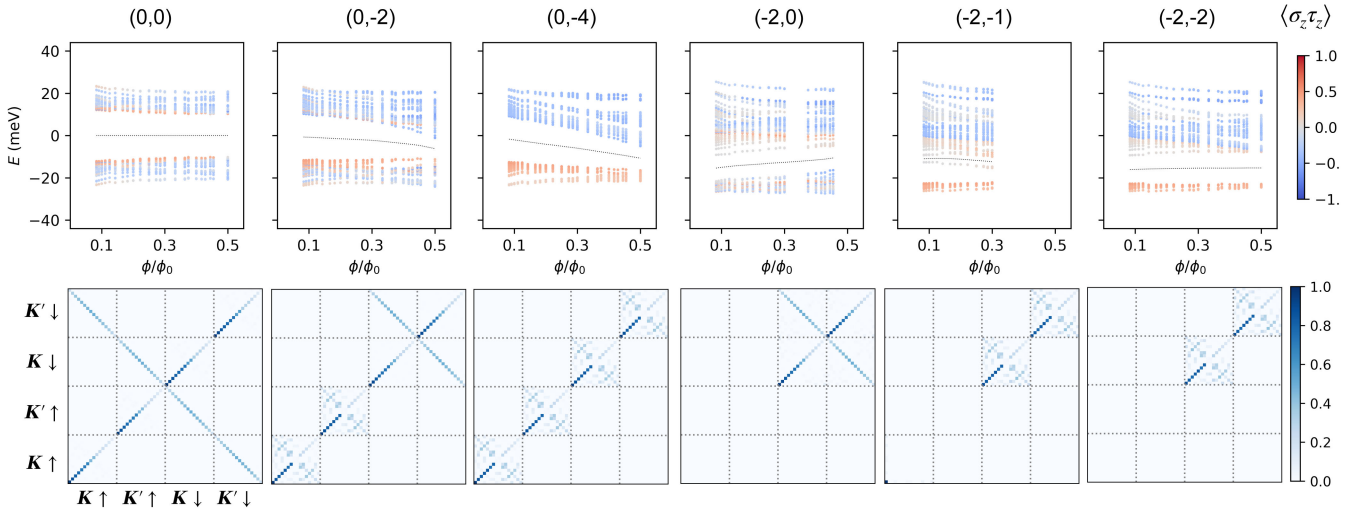

FIG. 5. Hartree-Fock excitation spectra (upper) and representative density matrices $|\hat{Q}_{\eta sr,\eta' s' r'}(\mathbf{0})|$ calculated at $\phi/\phi_0 = 1/8$ (lower) along (0,0), $(0,-2)$, $(0,-4)$, $(-2,0)$, $(-2,-1)$, and $(-2,-2)$, calculated for 1.20° in the absence of heterostrain. Electronic states below the dashed lines in the upper panel are occupied, and the color coding represents the averaged $\sigma_z\tau_z$ of every single-electron state. In $(-2,0)$ and $(-2,-1)$ excitation spectra at several ϕ/ϕ_0 are omitted in the plot, because they are states of different characters, due to either Landau fan crossing or the B-induced phase transitions as shown in Fig. 2(e). The density matrix structure for each column is as follows: Along (0,0) and $(-2,0)$, the occupied electronic states form an IVC state, between opposite spin species along (0,0), and between the spin $\downarrow$ species along $(0,-2)$ which is favored by Zeeman splitting. Along $(0,-4)$ and $(-2,-2)$, they are the CHF states. Along $(0,-2)$, it is a partial IVC state with IVC in the spin $\downarrow$ sector and a net Chern -2 valley-polarized state in the spin $\uparrow$ sector. Along $(-2,-1)$, it is a valley- and spin-polarized state, populating one extra LL on top of the $(-2,-2)$ CHF state.

state is described by adding one Landau level worth of electrons on top of a CHF ground state along $(-2,-2)$ rather than adding one Landau level worth of holes to an IVC state along $(-2,0)$. The latter state is metastable at 1.2° but is the Hartree-Fock ground state at 1.05°, as illustrated in Figs. 2(e) and 2(f). Our results at twist angle 1.2° therefore capture the most salient features of the experiments in Refs. [12,18].

It is also interesting to note that, at finite B, the (0,0) IVC state mixes opposite spin species. Within our numerics we can find an IVC state which mixes the same spin species, which has a slightly higher energy. Nevertheless, we find that the energetic difference between these two IVC states grows as B increases. For example, at $\phi/\phi_0 = 1/8$ the energy difference between these two states is about 0.02 meV per moiré unit cell but grows to about 0.4 meV at $\phi/\phi_0 = 5/11$.

F. Heavy-light dichotomy

As demonstrated in both Figs. 1 (strained) and 2 (unstrained), a notable feature of the finite B phase diagram is that the main gapped Chern states point *away* from the CNP as B increases, e.g., along $(s,t) = \pm(1,3)$, $\pm(2,2)$, and $\pm(3,1)$. On the other hand, with a few exceptions, Chern states pointing toward the CNP with a big gap are largely missing, e.g., along $(s,t) = \pm(-1,3)$, $\pm(-2,2)$, and $\pm(-3,1)$.

As we show in the previous section, at 1.05°, at low B, and in the absence of heterostrain, this can be understood from the Landau quantization [48,58] of the strong coupling single-particle excitation spectra of the flavor symmetry-breaking ground states at $B = 0$ [60,61]. At integer fillings on the hole-doped side of the CNP, a doped hole (i.e., moving away from CNP) has a light mass, leading to well-separated LLs (large cyclotron frequency) in relatively low B. In contrast, a doped electron (i.e., moving toward the CNP) has a heavy mass, and the LLs are much more densely spaced at a comparable B. While this explanation holds at low B for 1.05° twist angle without heterostrain, Figs. 1 and 2 show that the main Landau fans point away from the CNP even at larger twist angles or when we include moderate heterostrain. Under such conditions, the strong coupling limit is not reached as can be seen by the absence of the correlated insulators at $B = 0$ or the presence of IKS states which do not saturate the sublattice-valley polarization [Figs. 4(a) and 4(b)].

In order to understand why this result persists away from the strong coupling, we start by focusing on 1.28° in the absence of heterostrain whose phase diagram is presented in Fig. 2(c). In Figs. 6(a)–6(c), the left columns show the Hartree-Fock spectra of the respective ground states at $B = 0$ and $n/n_s = -1,-2,-3$. These ground states preserve the valley $U_v(1)$, spin $U_s(1)$, C_{3z}, and $C_{2z}T$ symmetries. As a result, the Dirac points (DPs) of any given valley and spin flavor are protected and located at the $\mathbf{K}$ point of the moiré Brillouin zone. Crucially, however, for all three fillings there is an exchange splitting (approximately 12 meV) between different flavors, as reflected in the relative energetic shift between the DPs of different valley and spin character. These ground states are all compressible, where the DPs are shifted above the Fermi energy, with the charge being compensated by the Fermi pockets from the exchange split bands. Moreover, there is a band renormalization effect for all flavors, reflected in the narrowing (sharpening) of the bands below (above) the DPs. The band renormalization becomes stronger as the filling is tuned to the band edge (e.g., $n/n_s = -3$). Such a band flattening effect has been discussed in the literature as a Hartree effect [24] (our calculation here also shows exchange splitting due to Fock terms). The second and third columns show the $B \neq 0$ Hartree-Fock spectra of the CHFs which share the same valley and spin quantum numbers as the $B = 0$ states and color coded in the same manner. It is evident that spectra of the CHFs can be smoothly extrapolated to the $B = 0$ Hartree-Fock dispersions, e.g., by matching the energies of the DP zLLs to DPs at $B = 0$. This demonstrates that the CHFs emerge from the respective compressible ground states at $B = 0$.

Generally, the heavy-light dichotomy at high twist angles (such as 1.28°) can be understood by examining the $B = 0$ dispersions. We address it using the CHF (or lack thereof) along $(-3,\pm1)$ as an example. As shown in Fig. 6(c), the CHF is formed by populating the Chern -1 group of magnetic subbands below the DP zLLs of a given valley and spin flavor (in this case, $\{\mathbf{K},\downarrow\}$ shown in the second column). However, Landau quantizing the $B = 0$ dispersions shows that CHF is not an energetically favorable state at infinitesimally weak B field, as the DP LLs of the $\mathbf{K},\downarrow$ are buried inside the dense LLs associated with the Fermi pockets (i.e., heavier electronic states due to band flattening) of the other three flavors. Only at larger B can the Chern -1 magnetic subband group be separated from the rest of the spectra due to the wide LL spacings of a linearly dispersing Dirac cone. This ties the finite B CHF along $(-3,-1)$ directly to the Landau quantizations of the $B = 0$ ground state. Conversely, the zLLs of the DPs cannot be separated from the dense LLs; therefore, the state along $(-3,1)$ is nearly compressible [unless intercepted by gapped states along another (s,t)]. The $B = 0$ and finite B correspondence can also explain why the critical field for the onset of CHFs along $(-3,-1)$ occurs at a lower B than $(-2,-2)$, which, in turn, occurs at a lower B than $(-1,-3)$. As n/n_s increases from -3 to -1, the flavor degeneracy of the DPs (marked by green or red crossings) increases, while the flavor degeneracy of the Fermi pockets—originating from the exchange split bands—decreases. As a result, the size of the Fermi pockets grows, and the bottom of these pockets sinks deeper below the DPs. A higher B is therefore necessary to separate the aforementioned Chern -1 group of magnetic subbands per flavor from the rest of the spectra.

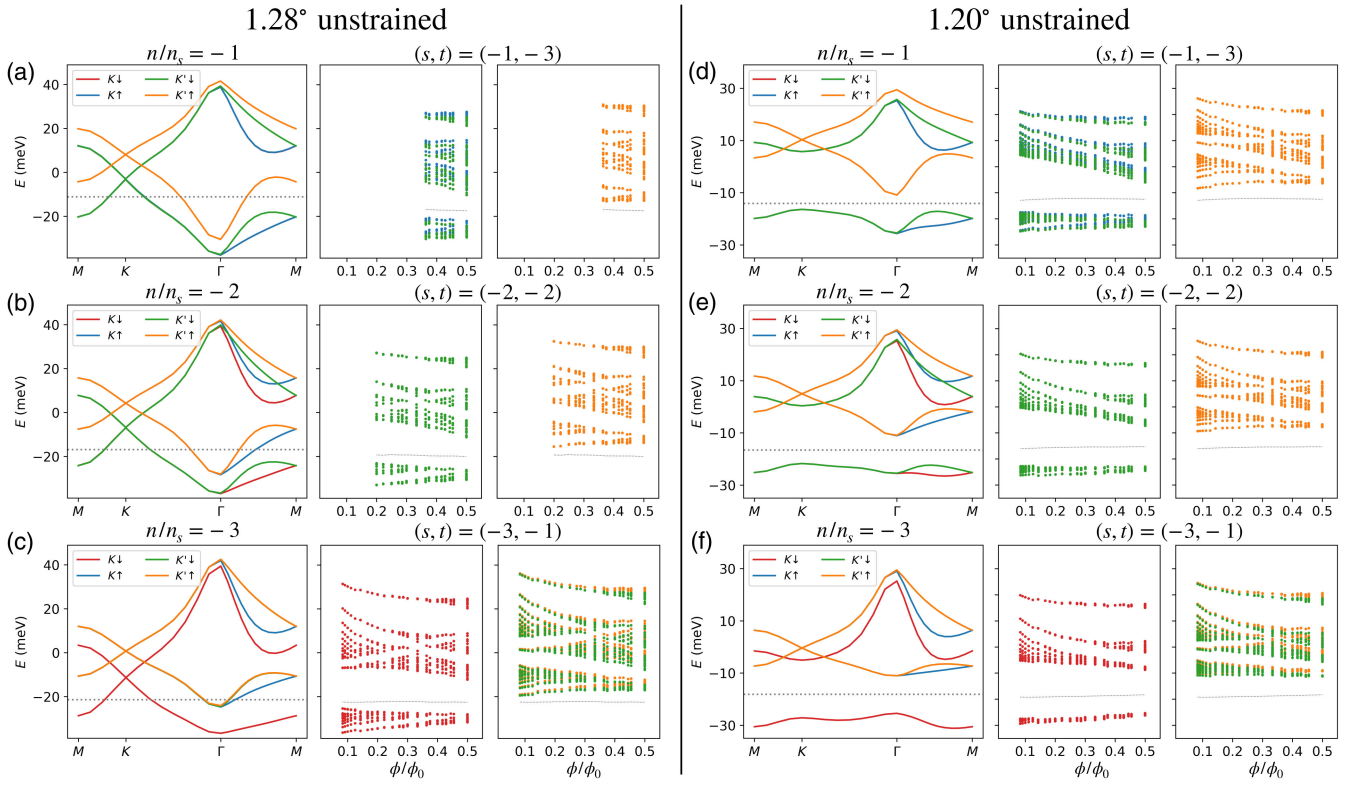

FIG. 6. Comparative study of $B = 0$ Hartree-Fock spectra at integer fillings $n/n_s = -1, -2, -3$ of states that preserve valley $U_v(1)$ and spin $U_s(1)$ symmetries and the $B \neq 0$ Hartree-Fock ground state spectra of CHFs along $(-1,-3)$, $(-2,-2)$, and $(-3,-1)$. The $B = 0$ states share the same valley and spin quantum numbers with the CHFs. (a)–(c) are at 1.20° twist angle and (d)–(f) are at 1.28°, all in the absence of heterostrain. At 1.20° the $B = 0$ states at $n/n_s = -1, -2$ are metastable, while the state at $n/n_s = -3$ is a stable ground state. They all break the $C_{2z}T$ symmetry and are incompressible Chern states with Chern numbers $-3, -2, -1$, respectively. Although not strictly in strong coupling, they are similar to the zCIs discussed in the strong coupling limit. The spectra of CHFs smoothly extrapolate to these states as B decreases even though some are metastable at $B = 0$. At 1.28°, the $B = 0$ states are stable ground states within our Hartree-Fock calculation, preserve $C_{2z}T$ and are compressible, but display sizable exchange splittings (approximately 12 meV) reflected in the relative energy shift of the Dirac cones of different valley and spin flavors. The spectra of CHFs also extrapolate to the spectra of the $B = 0$ states, albeit with some differences such as the exact locations of the zLLs of the exchange split Dirac cones. In (a) and (d), the $\{\mathbf{K}, \downarrow\}$ states (red) are hidden behind $\{\mathbf{K}, \uparrow\}$ (blue) at $B = 0$ and hidden behind $\{\mathbf{K}', \downarrow\}$ at $B \neq 0$. In (b) and (e) at $B \neq 0$, the spectrum of $\{\mathbf{K}, \downarrow\}$ (red) is hidden behind $\{\mathbf{K}', \downarrow\}$ (green), while that of $\{\mathbf{K}, \uparrow\}$ (blue) behind $\{\mathbf{K}', \uparrow\}$ (orange). In (c) and (f) and finite B, $\{\mathbf{K}, \uparrow\}$ (blue) states are hidden behind $\{\mathbf{K}', \uparrow\}$ (orange).

Next, we focus on 1.20° in the absence of heterostrain, where interaction effects are stronger than at 1.28°, with the CHFs along $(-3,-1)$, $(-2,-2)$, and $(-1,-3)$ all persisting down to the lowest magnetic flux ratio studied in this work. The finite B phase diagram is presented in Fig. 2(e), and the comparisons to $B = 0$ states are presented in Figs. 6(d)–6(f). These $B = 0$ states are obtained by enforcing the valley $U_v(1)$ and spin $U_s(1)$ symmetries and share the same valley and spin quantum numbers as the respective CHFs at finite B. While the state at $n/n_s = -3$ is the Hartree-Fock ground state, states at $n/n_s = -2, -1$ are metastable. Comparing the $B = 0$ and finite B spectra, we conclude that the CHFs originate from the Landau quantization of these $B = 0$ bands. A notable difference compared to 1.28° is that the $C_{2z}T$ symmetry is spontaneously broken at all $n/n_s = -3, -2, -1$, making them (meta)stable and gapped zCIs (with Chern numbers $\pm 1, \pm 2, \pm 3$, respectively), analogous to those discussed in the strong coupling limit [32,33]. Given that the $B = 0$ states at $n/n_s = -2, -1$ are metastable, at very low B, these CHFs must lose to populating LLs of the excitation spectra of the respective true ground states (with IVC order; see Fig. S20 [45]), likely via a first-order phase transition. This is in contrast to higher twist angles (e.g., 1.28°) where there are no competing zCI states nearby.

We finally address the heavy-light dichotomy for the calculations performed with 0.2% of uniaxial heterostrain. Because of competing Chern 0 IKS states (gapped or compressible) which persist to higher twist angles, it is challenging to find the $B = 0$ metastable states from which the finite B CCIs descend, as we can in the absence of heterostrain. We therefore postpone tying the finite B and $B = 0$ physics to a future work. Here, we instead provide an intuitive picture by examining Hartree-Fock spectra directly

at finite B. We use CCIs (or lack thereof) along $(-3,\pm 1)$ at 1.28° twist angle as an example. Along $(-3,-1)$, both CHF and IKS predominantly involve the lower Chern -1 group of the noninteracting magnetic subbands, separated from the zLLs and the upper Chern -1 group by a gap [see Fig. 3(a) for 1.2°; at 1.28°, the structure of the magnetic subbands is qualitatively similar]. The bandwidth of the lower Chern -1 group narrows upon increasing B, creating a favorable condition for symmetry-breaking states (either CHF or IKS) driven by Coulomb interactions [15]. Along $(-3,1)$, to get a similar flavor symmetry-breaking state, one would involve both the lower Chern -1 group and the two zLLs. However, as B increases, this Chern $+1$ composite of magnetic subbands has an increasing bandwidth, making it energetically more costly to break the valley and spin flavor symmetry. Conversely, it is more energetically favorable to populate two extra LLs from the nearby, exchange split, group of states on top of the $(-3,-1)$ state. Because of band flattening effect discussed above, an added electron to the bottom of the spectra of a given valley and spin flavor on the hole side of the CNP is heavy and reflected as nearly compressible along $(-3,1)$. This is further supported numerically from Fig. S4 [45], where the spectra above the gap at $(-3,-1)$ (gray) do not have well-separated LLs. The finite B perspective presented here complements the perspective of tying finite B to $B=0$ (meta)stable states and relies on the same Hartree-Fock effects of band (magnetic subband) renormalizations and exchange splitting.

At low twist angles in the presence of heterostrain, such as 1.20° and 1.05° shown in Figs. 1(e) and 1(f), the gapped IKS states along $(-3,-1)$, $(-2,-2)$, and $(-1,-3)$ remain robust down to the lowest magnetic flux ratio studied in this work, while gapped Chern 0 IKS states along $(-3,0)$ [both $(-3,0)$ and $(-2,0)$ at 1.05°] are also found. Moreover, we find that at 1.05° the IKS wave vectors of these two classes of IKS states are very different (approximately $\frac{1}{2}\mathbf{g}_1$ for Chern-0 IKS and approximately $\frac{1}{q}\mathbf{g}_2$ for IKS carrying a Chern number). Given the earlier discussions of competing zCI and IVC states in the absence of heterostrain and at lower twist angles, it is tempting to conjecture that the gapped IKS states along $(-3,-1)$, $(-2,-2)$, and $(-1,-3)$ may descend from $B=0$ "topological IKS" (tIKS) states which break the $C_{2z}T$ symmetry, i.e., a distinct IKS state from those reported in the literature [38]. Should they exist, the tIKS state must be metastable at $B=0$ and energetically unfavorable compared to the IKS state that preserves $C_{2z}T$. We leave more elaborate analysis of such a conjecture to future studies.

G. Additional CCIs

Besides the aforementioned CCIs, we also find additional correlated insulating states in the phase diagram both with and without heterostrain, as shown in Figs. 1 and 2, respectively.

In the presence of heterostrain, the most prominent states emanate from the CNP and are identified as quantum Hall ferromagnetic states (QHFMs) within the zLLs of the energetically split Dirac cones [62–64] (see Fig. S7 [45]). QHFMs emanating from the band minimum ($n/n_s=-4$) are well developed at 1.38° but become progressively weaker as the angle decreases (see Fig. S6 [45]). Moreover, at higher ϕ/ϕ_0 a gapped state with $(s,t)=(-2,0)$ is observed in Figs. 1(a)–1(c). We identify it as a QSH insulator due to strong spin splitting near $\phi/\phi_0=1/2$, as demonstrated in the noninteracting Hofstadter spectra in Fig. S1 and representative density matrices in Fig. S8 [45]. At 1.05°, we also find CCIs with fractional s along $(-2/3,-3)$, $(-1/2,-3)$, and $(-3/2,-2)$; see Fig. 1(f). These states break magnetic translation symmetry. We identify them as striped states with period m along the $\mathbf{L}_2$ direction, such that the density matrix is invariant under $(\hat{t}_{\mathbf{L}_2})^m$. Their respective density matrices are shown in Fig. S9 [45]. We use the electron occupation number of the lower zLL [see, e.g., Fig. 3(a)] in valley $\mathbf{K}$ and for spin $\downarrow$ to illustrate the striped states. We define it as $n_0(\mathbf{k})$ and show its momentum dependence in the magnetic Brillouin zone at $\phi/\phi_0=1/6$ for $(-2/3,-3)$, $(-1/2,-3)$, and $(-3/2,-2)$ in Figs. 7(a), 7(b), and 7(c), respectively. At $(-1/2,-3)$ and $(-3/2,-2)$, the fractional part of s corresponds to half filling of a valley and spin flavor, and we identify the period of the striped state as $m=2$. At $(-2/3,-3)$, the fractional part of s corresponds to two-thirds filling of a flavor, and we identify the stripe period as $m=3$. While some of the fractional s CCIs show intervalley coherence and others show valley or spin polarization, the energy difference between these two kinds of states are about 0.05 meV per moiré unit cell. Within our numerical accuracy, we cannot say with certainty if either will be observed in future experimental works. Furthermore, we are also limited to probe striped states only along the $\mathbf{L}_2$ direction, but not

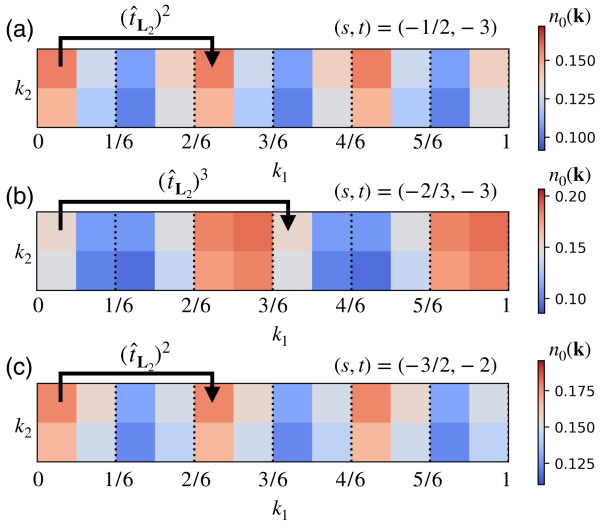

FIG. 7. Occupation number $n_0(\mathbf{k})$ of the lower zLL of the noninteracting spectra in valley $\mathbf{K}$ and for spin $\downarrow$. Results are obtained at 1.05° for correlated Chern insulating states with fractional s, marked by the dashed lines in Fig. 1(f).

striped states along $\mathbf{L}_1$ or checkerboard states modulating along both directions. Nevertheless, it is clear that states with broken magnetic translation symmetries (being striped or checkerboard states) are more energetically favorable than states that preserve them (or IKS states that preserve modified magnetic translation symmetries). More careful studies of fractional s states are beyond the scope of the present work and left for the future. Reference [14] observed fractional s CCIs in h-BN aligned TBG devices and presented a qualitative argument based on translation symmetry-breaking phases at $B = 0$. Here, our results demonstrate that they can be stabilized purely due to interactions and without h-BN alignment.

In the absence of heterostrain and large twist angles, we identify gapped states emanating from the band minimum as QHFMs similar to the strained case (see Fig. S13 [45]). However, the most prominent gapped states emanating from the CNP are no longer QHFMs even at the largest twist angle studied. As alluded to in Sec. III E, the CNP develops a small but finite correlation gap even at 1.38°, supported by separate $B = 0$ Hartree-Fock studies. However, the energy minimum of electronlike excitations (or maximum of holelike excitations) remains at the hexagon corners of the moiré Brillouin zone. As the twist angle decreases, QHFMs emanating from the band minimum fade away similar to the cases in the presence of heterostrain, the size of the IVC gap at CNP grows, and Coulomb interaction hybridizes electronic states further from the vicinity of the Dirac cones of the noninteracting band. This eventually leads to "inverted" excitation spectra at the magic angle 1.05°, with the energy minimum of electronlike excitations shifted to the Γ point of the moiré Brillouin zone. Additionally, as in the strained case, fractional s CCIs are also found at the magic angle but persist to higher twist angles compared to strained case (see Fig. S16 [45]).

IV. CONCLUSION

In summary, by performing a comprehensive self-consistent Hartree-Fock study of the continuum Bistritzer-MacDonald model in finite magnetic fields, we unravel the nature of the prominent correlated Chern insulators observed in a wide range of TBG experiments. For realistic heterostrain, these correlated Chern insulators are stabilized at higher magnetic fields and correspond to valley and spin polarizations of the interaction-renormalized magnetic subbands that we dub correlated Hofstadter ferromagnets. Upon lowering magnetic field, the CHFs become energetically less favored, losing to gapped states with intervalley coherence. In the absence of heterostrain and at higher magnetic fields, the CHF crosses over to the strong coupling Chern insulating states as the twist angle decreases. At lower fields, competing states with intervalley coherence become more energetically favored, and the transition is marked by a collapse of the averaged sublattice polarization per occupied single-electron state.

Our calculations also predict additional gapped correlated insulating states beyond the $(s,t) = (0,\pm4),\pm(1,3),\pm(2,2),\pm(3,1)$ sequence, notably the striped states at fractional s. Given that our calculations have direct access to the interaction renormalized single-electron excitation spectra at a given filling and magnetic field (see Fig. S10 [45]), comparisons with experiments such as STM can be made to facilitate the characterization of the panoply of correlated insulating states.

ACKNOWLEDGMENTS

X. W. and O. V. acknowledge invaluable discussions with B. Andrei Bernevig, Cyprian Lewandowski, Joe Finney, Minhao He, Jian Kang, Erez Berg, Nick Bultinck, Tomohiro Soejima, and Tianle Wang. X. W. acknowledges financial support from the Gordon and Betty Moore Foundation's EPiQS Initiative Grant No. GBMF11070, National High Magnetic Field Laboratory through National Science Foundation (NSF) Grant No. DMR-2128556, and the State of Florida. O. V. was supported by NSF Grant No. DMR-1916958 and is partially funded by the Gordon and Betty Moore Foundation's EPiQS Initiative Grant No. GBMF11070. Most of the computing for this project was performed on the HPC at the Research Computing Center at the Florida State University (FSU).

[1] E. Y. Andrei and A. H. MacDonald, *Graphene bilayers with a twist*, Nat. Mater. **19**, 1265 (2020).
[2] L. Balents, C. R. Dean, D. K. Efetov, and A. F. Young, *Superconductivity and strong correlations in moiré flat bands*, Nat. Phys. **16**, 725 (2020).
[3] R. Bistritzer and A. H. MacDonald, *Moiré bands in twisted double-layer graphene*, Proc. Natl. Acad. Sci. U.S.A. **108**, 12233 (2011).
[4] Y. Cao, V. Fatemi, A. Demir, S. Fang, S. L. Tomarken, J. Y. Luo, J. D. Sanchez-Yamagishi, K. Watanabe, T. Taniguchi, E. Kaxiras, R. C. Ashoori, and P. Jarillo-Herrero, *Correlated insulator behaviour at half-filling in magic-angle graphene superlattices*, Nature (London) **556**, 80 (2018).
[5] Y. Cao, V. Fatemi, S. Fang, K. Watanabe, T. Taniguchi, E. Kaxiras, and P. Jarillo-Herrero, *Unconventional superconductivity in magic-angle graphene superlattices*, Nature (London) **556**, 43 (2018).
[6] S. L. Tomarken, Y. Cao, A. Demir, K. Watanabe, T. Taniguchi, P. Jarillo-Herrero, and R. C. Ashoori, *Electronic compressibility of magic-angle graphene superlattices*, Phys. Rev. Lett. **123**, 046601 (2019).
[7] J. M. Park, Y. Cao, K. Watanabe, T. Taniguchi, and P. Jarillo-Herrero, *Flavour Hund's coupling, Chern gaps and charge diffusivity in moiré graphene*, Nature (London) **592**, 43 (2021).
[8] Y. Xie, B. Lian, B. Jäck, X. Liu, C.-L. Chiu, K. Watanabe, T. Taniguchi, B. A. Bernevig, and A. Yazdani, *Spectroscopic*

signatures of many-body correlations in magic-angle twisted bilayer graphene, Nature (London) **572**, 101 (2019).

[9] M. Yankowitz, S. Chen, H. Polshyn, Y. Zhang, K. Watanabe, T. Taniguchi, D. Graf, A. F. Young, and C. R. Dean, *Tuning superconductivity in twisted bilayer graphene*, Science **363**, 1059 (2019).

[10] A. L. Sharpe, E. J. Fox, A. W. Barnard, J. Finney, K. Watanabe, T. Taniguchi, M. A. Kastner, and D. Goldhaber-Gordon, *Emergent ferromagnetism near three-quarters filling in twisted bilayer graphene*, Science **365**, 605 (2019).

[11] K. P. Nuckolls, M. Oh, D. Wong, B. Lian, K. Watanabe, T. Taniguchi, B. A. Bernevig, and A. Yazdani, *Strongly correlated Chern insulators in magic-angle twisted bilayer graphene*, Nature (London) **588**, 610 (2020).

[12] K. P. Nuckolls, R. L. Lee, M. Oh, D. Wong, T. Soejima, J. P. Hong, D. Călugăru, J. Herzog-Arbeitman, B. A. Bernevig, K. Watanabe, T. Taniguchi, N. Regnault, M. P. Zaletel, and A. Yazdani, *Quantum textures of the many-body wavefunctions in magic-angle graphene*, Nature (London) **620**, 525 (2023).

[13] A. T. Pierce, Y. Xie, J. M. Park, E. Khalaf, S. H. Lee, Y. Cao, D. E. Parker, P. R. Forrester, S. Chen, K. Watanabe, T. Taniguchi, A. Vishwanath, P. Jarillo-Herrero, and A. Yacoby, *Unconventional sequence of correlated Chern insulators in magic-angle twisted bilayer graphene*, Nat. Phys. **17**, 1210 (2021).

[14] Y. Xie, A. T. Pierce, J. M. Park, D. E. Parker, E. Khalaf, P. Ledwith, Y. Cao, S. H. Lee, S. Chen, P. R. Forrester, K. Watanabe, T. Taniguchi, A. Vishwanath, P. Jarillo-Herrero, and A. Yacoby, *Fractional Chern insulators in magic-angle twisted bilayer graphene*, Nature (London) **600**, 439 (2021).

[15] Y. Saito, J. Ge, L. Rademaker, K. Watanabe, T. Taniguchi, D. A. Abanin, and A. F. Young, *Hofstadter subband ferromagnetism and symmetry-broken Chern insulators in twisted bilayer graphene*, Nat. Phys. **17**, 478 (2021).

[16] J. Yu, B. A. Foutty, Z. Han, M. E. Barber, Y. Schattner, K. Watanabe, T. Taniguchi, P. Phillips, Z.-X. Shen, S. A. Kivelson, and B. E. Feldman, *Correlated Hofstadter spectrum and flavour phase diagram in magic-angle twisted bilayer graphene*, Nat. Phys. **18**, 825 (2022).

[17] J. C. Hoke, Y. Li, J. May-Mann, K. Watanabe, T. Taniguchi, B. Bradlyn, T. L. Hughes, and B. E. Feldman, *Uncovering the spin ordering in magic-angle graphene via edge state equilibration*, arXiv:2309.06583.

[18] X. Lu, P. Stepanov, W. Yang, M. Xie, M. A. Aamir, I. Das, C. Urgell, K. Watanabe, T. Taniguchi, G. Zhang, A. Bachtold, A. H. MacDonald, and D. K. Efetov, *Superconductors, orbital magnets and correlated states in magic-angle bilayer graphene*, Nature (London) **574**, 653 (2019).

[19] I. Das, X. Lu, J. Herzog-Arbeitman, Z.-D. Song, K. Watanabe, T. Taniguchi, B. A. Bernevig, and D. K. Efetov, *Symmetry-broken Chern insulators and Rashba-like Landau-level crossings in magic-angle bilayer graphene*, Nat. Phys. **17**, 710 (2021).

[20] M. Serlin, C. L. Tschirhart, H. Polshyn, Y. Zhang, J. Zhu, K. Watanabe, T. Taniguchi, L. Balents, and A. F. Young, *Intrinsic quantized anomalous Hall effect in a moiré heterostructure*, Science **367**, 900 (2020).

[21] P. Stepanov, M. Xie, T. Taniguchi, K. Watanabe, X. Lu, A. H. MacDonald, B. A. Bernevig, and D. K. Efetov, *Competing zero-field Chern insulators in superconducting twisted bilayer graphene*, Phys. Rev. Lett. **127**, 197701 (2021).

[22] S. Wu, Z. Zhang, K. Watanabe, T. Taniguchi, and E. Y. Andrei, *Chern insulators, van Hove singularities and topological flat bands in magic-angle twisted bilayer graphene*, Nat. Mater. **20**, 488 (2021).

[23] Y. Choi, H. Kim, Y. Peng, A. Thomson, C. Lewandowski, R. Polski, Y. Zhang, H. S. Arora, K. Watanabe, T. Taniguchi, J. Alicea, and S. Nadj-Perge, *Correlation-driven topological phases in magic-angle twisted bilayer graphene*, Nature (London) **589**, 536 (2021).

[24] Y. Choi, H. Kim, C. Lewandowski, Y. Peng, A. Thomson, R. Polski, Y. Zhang, K. Watanabe, T. Taniguchi, J. Alicea, and S. Nadj-Perge, *Interaction-driven band flattening and correlated phases in twisted bilayer graphene*, Nat. Phys. **17**, 1375 (2021).

[25] S. Grover, M. Bocarsly, A. Uri, P. Stepanov, G. Di Battista, I. Roy, J. Xiao, A. Y. Meltzer, Y. Myasoedov, K. Pareek, K. Watanabe, T. Taniguchi, B. Yan, A. Stern, E. Berg, D. K. Efetov, and E. Zeldov, *Chern mosaic and Berry-curvature magnetism in magic-angle graphene*, Nat. Phys. **18**, 885 (2022).

[26] A. Uri, S. Grover, Y. Cao, J. A. Crosse, K. Bagani, D. Rodan-Legrain, Y. Myasoedov, K. Watanabe, T. Taniguchi, P. Moon, M. Koshino, P. Jarillo-Herrero, and E. Zeldov, *Mapping the twist-angle disorder and Landau levels in magic-angle graphene*, Nature (London) **581**, 47 (2020).

[27] H. C. Po, L. Zou, T. Senthil, and A. Vishwanath, *Faithful tight-binding models and fragile topology of magic-angle bilayer graphene*, Phys. Rev. B **99**, 195455 (2019).

[28] Z. Song, Z. Wang, W. Shi, G. Li, C. Fang, and B. A. Bernevig, *All magic angles in twisted bilayer graphene are topological*, Phys. Rev. Lett. **123**, 036401 (2019).

[29] N. Bultinck, E. Khalaf, S. Liu, S. Chatterjee, A. Vishwanath, and M. P. Zaletel, *Ground state and hidden symmetry of magic-angle graphene at even integer filling*, Phys. Rev. X **10**, 031034 (2020).

[30] J. Kang and O. Vafek, *Non-Abelian Dirac node braiding and near-degeneracy of correlated phases at odd integer filling in magic-angle twisted bilayer graphene*, Phys. Rev. B **102**, 035161 (2020).

[31] Y.-H. Zhang, D. Mao, and T. Senthil, *Twisted bilayer graphene aligned with hexagonal boron nitride: Anomalous Hall effect and a lattice model*, Phys. Rev. Res. **1**, 033126 (2019).

[32] N. Bultinck, S. Chatterjee, and M. P. Zaletel, *Mechanism for anomalous Hall ferromagnetism in twisted bilayer graphene*, Phys. Rev. Lett. **124**, 166601 (2020).

[33] B. Lian, Z.-D. Song, N. Regnault, D. K. Efetov, A. Yazdani, and B. A. Bernevig, *Twisted bilayer graphene. IV. Exact insulator ground states and phase diagram*, Phys. Rev. B **103**, 205414 (2021).

[34] J. Liu and X. Dai, *Theories for the correlated insulating states and quantum anomalous Hall effect phenomena in twisted bilayer graphene*, Phys. Rev. B **103**, 035427 (2021).

[35] M. Xie and A. H. MacDonald, *Nature of the correlated insulator states in twisted bilayer graphene*, Phys. Rev. Lett. **124**, 097601 (2020).

[36] T. Soejima, D. E. Parker, N. Bultinck, J. Hauschild, and M. P. Zaletel, *Efficient simulation of moiré materials using the density matrix renormalization group*, Phys. Rev. B **102**, 205111 (2020).

[37] Z. Bi, N. F. Q. Yuan, and L. Fu, *Designing flat bands by strain*, Phys. Rev. B **100**, 035448 (2019).

[38] Y. H. Kwan, G. Wagner, T. Soejima, M. P. Zaletel, S. H. Simon, S. A. Parameswaran, and N. Bultinck, *Kekulé spiral order at all nonzero integer fillings in twisted bilayer graphene*, Phys. Rev. X **11**, 041063 (2021).

[39] X. Wang, J. Finney, A. L. Sharpe, L. K. Rodenbach, C. L. Hsueh, K. Watanabe, T. Taniguchi, M. A. Kastner, O. Vafek, and D. Goldhaber-Gordon, *Unusual magnetotransport in twisted bilayer graphene from strain-induced open Fermi surfaces*, Proc. Natl. Acad. Sci. U.S.A. **120**, e2307151120 (2023).

[40] H. C. Po, L. Zou, A. Vishwanath, and T. Senthil, *Origin of Mott insulating behavior and superconductivity in twisted bilayer graphene*, Phys. Rev. X **8**, 031089 (2018).

[41] J. Kang and O. Vafek, *Strong coupling phases of partially filled twisted bilayer graphene narrow bands*, Phys. Rev. Lett. **122**, 246401 (2019).

[42] O. Vafek and J. Kang, *Lattice model for the Coulomb interacting chiral limit of magic-angle twisted bilayer graphene: Symmetries, obstructions, and excitations*, Phys. Rev. B **104**, 075143 (2021).

[43] S. Liu, E. Khalaf, J. Y. Lee, and A. Vishwanath, *Nematic topological semimetal and insulator in magic-angle bilayer graphene at charge neutrality*, Phys. Rev. Res. **3**, 013033 (2021).

[44] F. Xie, J. Kang, B. A. Bernevig, O. Vafek, and N. Regnault, *Phase diagram of twisted bilayer graphene at filling factor* $\nu = \pm 3$, Phys. Rev. B **107**, 075156 (2023).

[45] See Supplemental Material at http://link.aps.org/supplemental/10.1103/PhysRevX.14.021042 for more details on theoretical modeling and supporting figures.

[46] I. Das, C. Shen, A. Jaoui, J. Herzog-Arbeitman, A. Chew, C.-W. Cho, K. Watanabe, T. Taniguchi, B. A. Piot, B. A. Bernevig, and D. K. Efetov, *Observation of reentrant correlated insulators and interaction-driven Fermi-surface reconstructions at one magnetic flux quantum per moiré unit cell in magic-angle twisted bilayer graphene*, Phys. Rev. Lett. **128**, 217701 (2022).

[47] J. M. B. Lopes dos Santos, N. M. R. Peres, and A. H. Castro Neto, *Graphene bilayer with a twist: Electronic structure*, Phys. Rev. Lett. **99**, 256802 (2007).

[48] X. Wang and O. Vafek, *Narrow bands in magnetic field and strong-coupling Hofstadter spectra*, Phys. Rev. B **106**, L121111 (2022).

[49] X. Wang and O. Vafek, *Revisiting Bloch electrons in a magnetic field: Hofstadter physics via hybrid Wannier states*, Phys. Rev. B **108**, 245109 (2023).

[50] B. A. Bernevig, Z.-D. Song, N. Regnault, and B. Lian, *Twisted bilayer graphene. III. Interacting hamiltonian and exact symmetries*, Phys. Rev. B **103**, 205413 (2021).

[51] O. Vafek and J. Kang, *Renormalization group study of hidden symmetry in twisted bilayer graphene with Coulomb interactions*, Phys. Rev. Lett. **125**, 257602 (2020).

[52] U. Zondiner, A. Rozen, D. Rodan-Legrain, Y. Cao, R. Queiroz, T. Taniguchi, K. Watanabe, Y. Oreg, F. von Oppen, A. Stern, E. Berg, P. Jarillo-Herrero, and S. Ilani, *Cascade of phase transitions and dirac revivals in magic-angle graphene*, Nature (London) **582**, 203 (2020).

[53] D. Wong, K. P. Nuckolls, M. Oh, B. Lian, Y. Xie, S. Jeon, K. Watanabe, T. Taniguchi, B. A. Bernevig, and A. Yazdani, *Cascade of electronic transitions in magic-angle twisted bilayer graphene*, Nature (London) **582**, 198 (2020).

[54] Y. Saito, F. Yang, J. Ge, X. Liu, T. Taniguchi, K. Watanabe, J. I. A. Li, E. Berg, and A. F. Young, *Isospin Pomeranchuk effect in twisted bilayer graphene*, Nature (London) **592**, 220 (2021).

[55] K. Hejazi, C. Liu, H. Shapourian, X. Chen, and L. Balents, *Multiple topological transitions in twisted bilayer graphene near the first magic angle*, Phys. Rev. B **99**, 035111 (2019).

[56] J. Herzog-Arbeitman, A. Chew, D. K. Efetov, and B. A. Bernevig, *Reentrant correlated insulators in twisted bilayer graphene at 25 t* $(2\pi$ *flux)*, Phys. Rev. Lett. **129**, 076401 (2022).

[57] J. Kang and O. Vafek, *Pseudomagnetic fields, particle-hole asymmetry, and microscopic effective continuum Hamiltonians of twisted bilayer graphene*, Phys. Rev. B **107**, 075408 (2023).

[58] K. Singh, A. Chew, J. Herzog-Arbeitman, B. A. Bernevig, and O. Vafek, *Topological heavy fermions in magnetic field*, arXiv:2305.08171.

[59] G. Tarnopolsky, A. J. Kruchkov, and A. Vishwanath, *Origin of magic angles in twisted bilayer graphene*, Phys. Rev. Lett. **122**, 106405 (2019).

[60] B. A. Bernevig, B. Lian, A. Cowsik, F. Xie, N. Regnault, and Z.-D. Song, *Twisted bilayer graphene. V. Exact analytic many-body excitations in Coulomb Hamiltonians: Charge gap, Goldstone modes, and absence of Cooper pairing*, Phys. Rev. B **103**, 205415 (2021).

[61] J. Kang, B. A. Bernevig, and O. Vafek, *Cascades between light and heavy fermions in the normal state of magic-angle twisted bilayer graphene*, Phys. Rev. Lett. **127**, 266402 (2021).

[62] K. Nomura and A. H. MacDonald, *Quantum Hall ferromagnetism in graphene*, Phys. Rev. Lett. **96**, 256602 (2006).

[63] M. Kharitonov, *Phase diagram for the* $\nu = 0$ *quantum Hall state in monolayer graphene*, Phys. Rev. B **85**, 155439 (2012).

[64] A. F. Young, C. R. Dean, L. Wang, H. Ren, P. Cadden-Zimansky, K. Watanabe, T. Taniguchi, J. Hone, K. L. Shepard, and P. Kim, *Spin and valley quantum Hall ferromagnetism in graphene*, Nat. Phys. **8**, 550 (2012).